Supporting Information

High-Performance Double Ion-buffering Reservoirs of Asymmetric Supercapacitors Based on Flower-like Co$_3$O$_4$-G>N-PEGm Microspheres and 3D rGO-CNT>N-PEGm Aerogels

Changwei Lai,[ab] Ying Sun,[a] Xueqin Zhang,[a] Hong Yang,[a] and Baoping Lin*[a]

[a]School of Chemistry and Chemical Engineering, Southeast University, Nanjing, 211189, P. R. China
[b]Anyang Institute of Technology, Anyang, 455000, P. R. China.

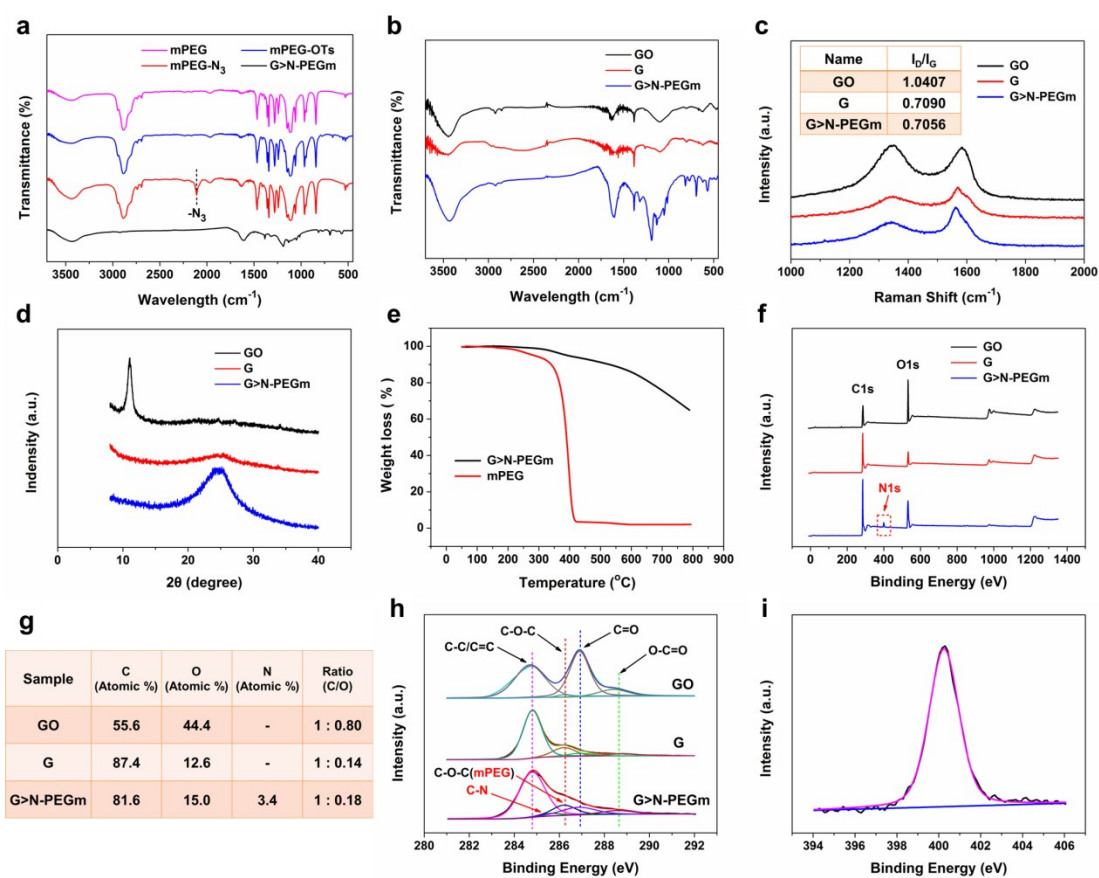* Corresponding author

E-mail: lbp@seu.edu.cn

Figure S1. (a-b) FT-IR spectra of mPEG, mPEG-OTs, mPEG-N$_3$, G>N-PEGm, GO and G. (c) Raman spectra of GO, G and G>N-PEGm (the inset shows the ratio of I$_D$/I$_G$). (d) XRD patterns of GO, G and G>N-PEGm. (e) TGA curves of G>N-PEGm and mPEG in N$_2$. (f) The fully scanned XPS spectra, (g) the C/O ratio and (h) C 1s high-resolution XPS spectra of GO, G and G>N-PEGm. (i) N 1s high-resolution XPS spectrum of G>N-PEGm
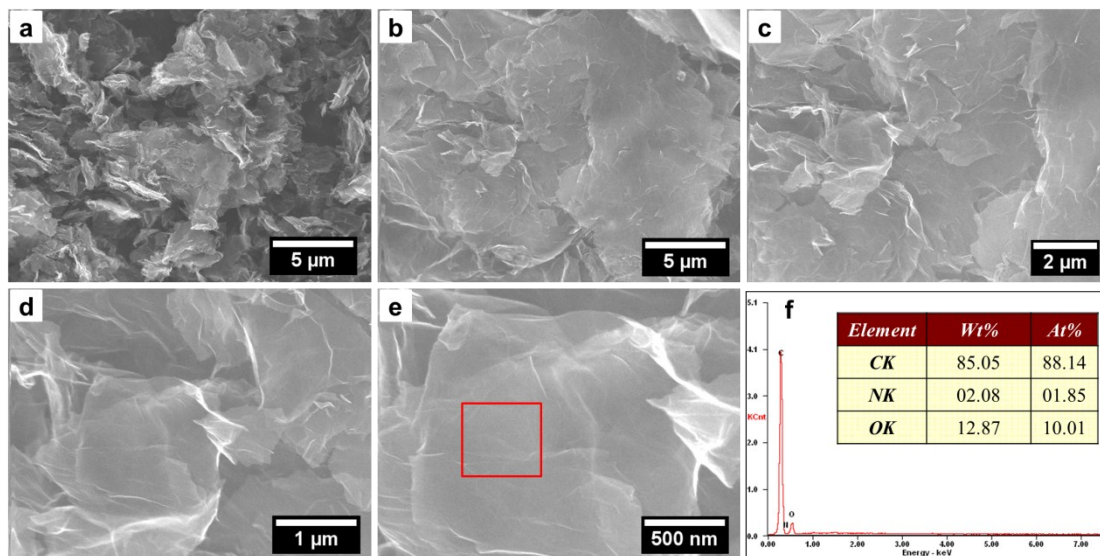
Figure S2. (a-e) Different magnification SEM images of G>N-PEGm nanosheets. (f) EDS spectrum of G>N-PEGm (the inset shows the ratio of elements).
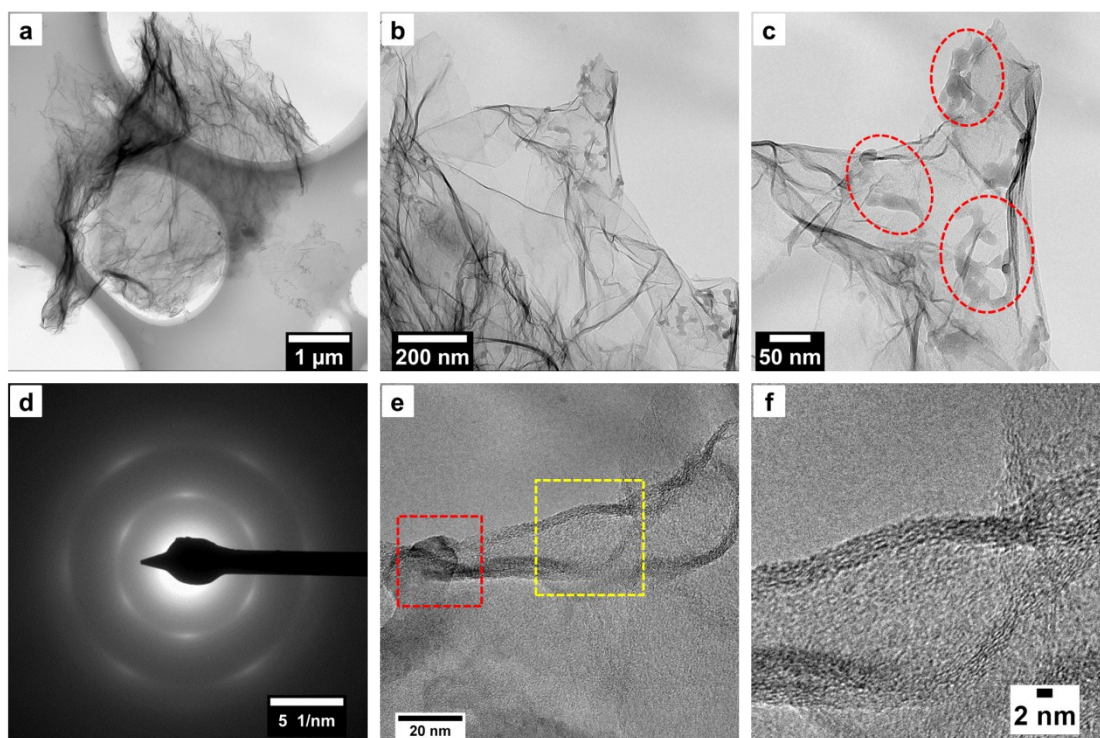

Figure S3. (a-c) Different magnification TEM images of G>N-PEGm nanosheets (the red rings in figure S3c show the aggregation of PEG polymer chains on the surface of the grapheme nanosheets). (d) SAED patterns and (e-f) HRTEM images of G>N-PEGm nanosheets.
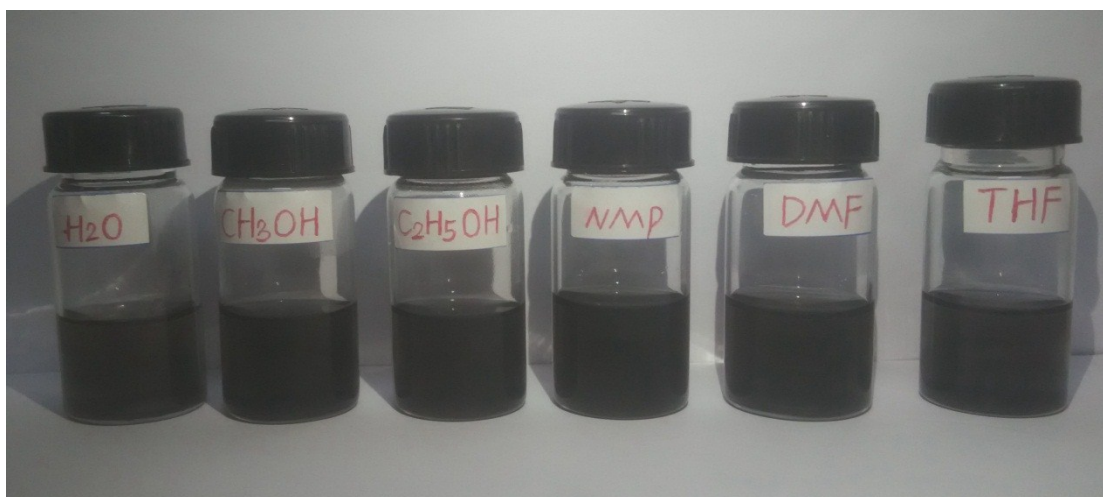
Figure S4. Photographs of G>N-PEGm nanosheets dispersed in water, methanol, ethanol, NMP, DMF and THF (respectively from left to right).
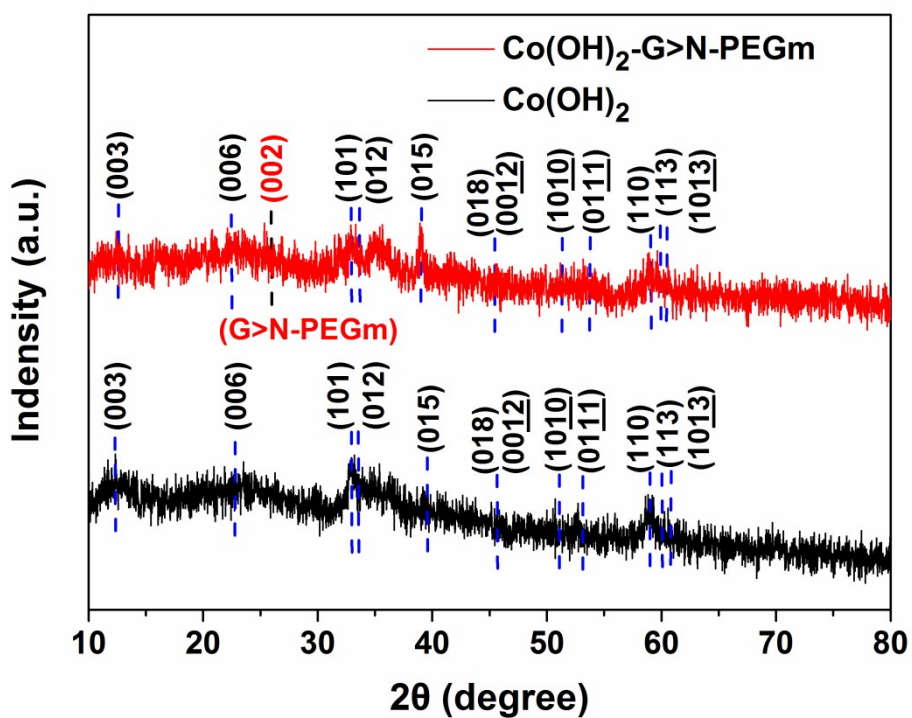

Figure S5. XRD patterns of the 3D flower-like hierarchical microspheres of $Co(OH)_2$ and $Co(OH)_2$-G>N-PEGm.
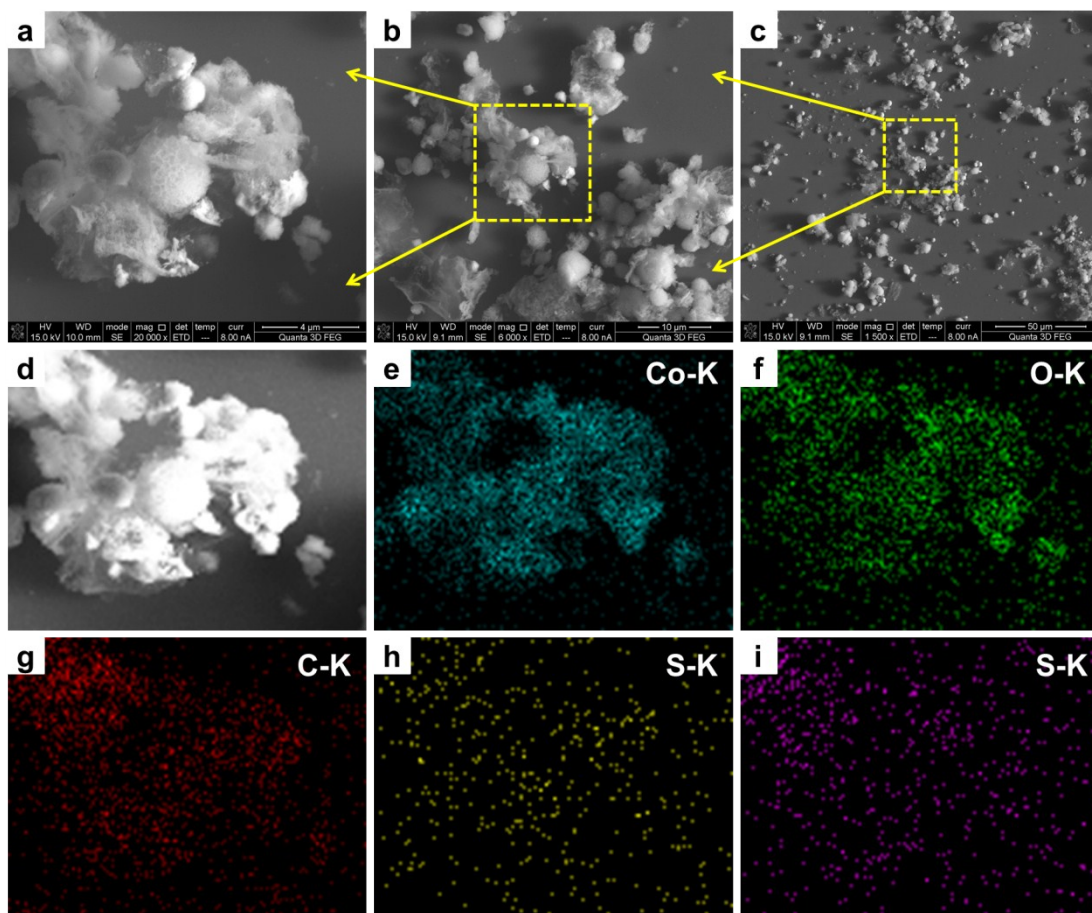
Figure S6. (a-c) Different magnification SEM images of Co(OH)$_2$-G>N-PEGm, (d-i) the EDS elemental mapping analysis of Co-L, O-K, C-K, S-K, and Cl-K for DBS-α-Co(OH)$_2$-G>N-PEGm flower spherses.

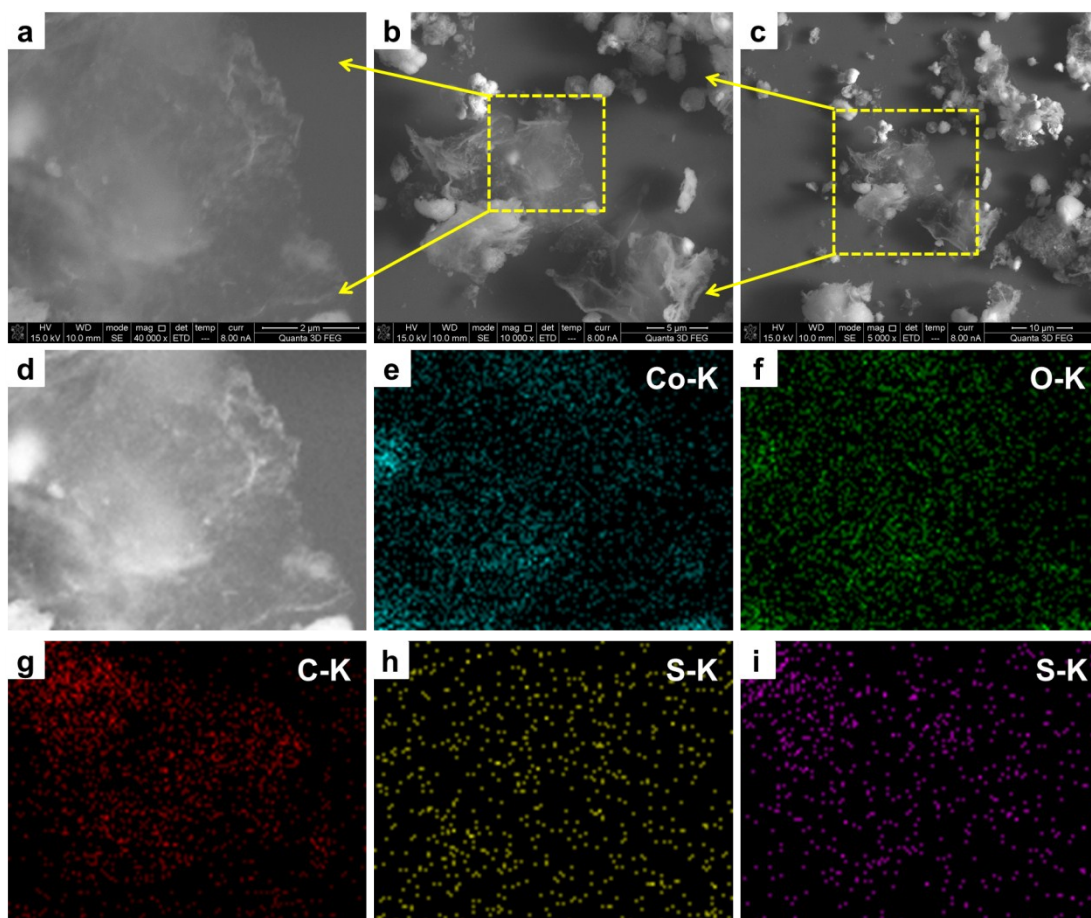**Figure S7.** (a-c) Different magnification SEM images of G>N-PEGm nanosheets in the Co(OH)$_2$-G>N-PEGm composites, (d-i) the EDS elemental mapping analysis of Co-L, O-K, C-K, S-K, and Cl-K for G>N-PEGm.

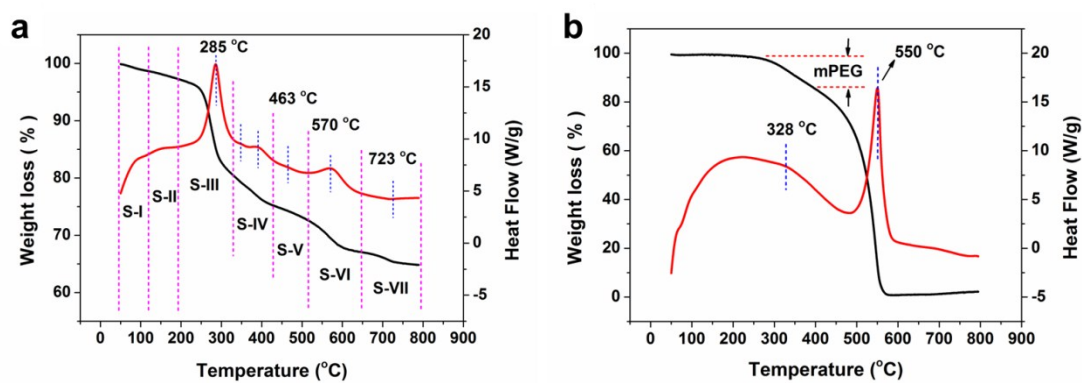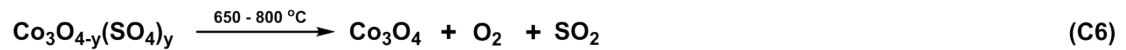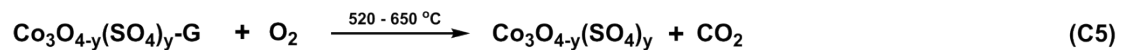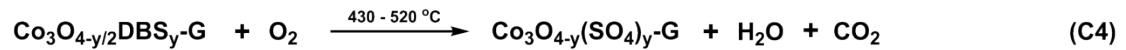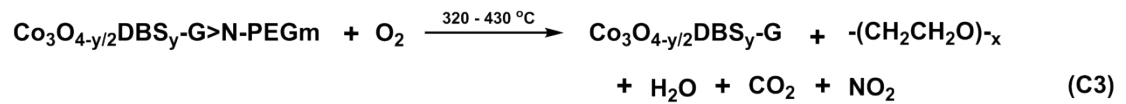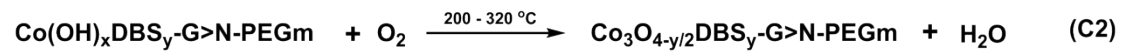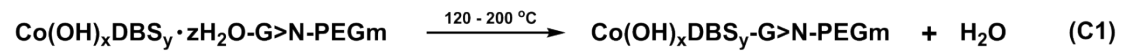**Figure S8.** (a) TGA-DSC curves of the 3D flower-like hierarchical microspheres DBS-Co(OH)$_2$-G>N-PEGm in air. (b) TGA-DSC curves of the G>N-PEGm nanosheets in air.

Table S1. Temperature ranges of TGA-DSC curves of the flower microspheres $Co(OH)_2$-G>N-PEGm composites in air.

Stage	Temperature range	Discussion	Chemical reaction	Weight loss range (%)	Weight loss (%)
S-I	50-120	Adsorbed surface water	-	99.9-98.7	1.2
S-II	120-200	Intercalated crystallization water	C1	98.7-97.4	1.3
S-III	200-320	Thermal oxidative decomposition of $Co(OH)_2$	C2	97.4-80.5	16.9
S-IV	320-430	Thermal oxidation of mPEG (on G>N-PEGm)	C3	80.5-75.3	5.2
S-V	430-520	Thermal oxidation of DBS	C4	75.3-72.6	2.7
S-VI	520-650	Thermal oxidation of G	C5	72.6-67.1	5.5
S-VII	650-800	Thermal oxidation of $CoSO_4$	C6	67.1-64.8	2.3

Chemical reactions in the stages of TGA-DSC curves of the flower microspheres $Co(OH)_2$-G>N-PEGm composites in air as follows:

$$Co(OH)_xDBS_y \cdot zH_2O\text{-}G\text{>}N\text{-}PEGm \xrightarrow{120-200\,^{\circ}C} Co(OH)_xDBS_y\text{-}G\text{>}N\text{-}PEGm + H_2O \qquad (C1)$$

$$Co(OH)_xDBS_y\text{-}G\text{>}N\text{-}PEGm + O_2 \xrightarrow{200-320\,^{\circ}C} Co_3O_{4-y/2}DBS_y\text{-}G\text{>}N\text{-}PEGm + H_2O \qquad (C2)$$

$$Co_3O_{4-y/2}DBS_y\text{-}G\text{>}N\text{-}PEGm + O_2 \xrightarrow{320-430\,^{\circ}C} Co_3O_{4-y/2}DBS_y\text{-}G + \text{-}(CH_2CH_2O)\text{-}_x$$
$$+ H_2O + CO_2 + NO_2 \qquad (C3)$$

$$Co_3O_{4-y/2}DBS_y\text{-}G + O_2 \xrightarrow{430-520\,^{\circ}C} Co_3O_{4-y}(SO_4)_y\text{-}G + H_2O + CO_2 \qquad (C4)$$

$$Co_3O_{4-y}(SO_4)_y\text{-}G + O_2 \xrightarrow{520-650\,^{\circ}C} Co_3O_{4-y}(SO_4)_y + CO_2 \qquad (C5)$$

$$Co_3O_{4-y}(SO_4)_y \xrightarrow{650-800\,^{\circ}C} Co_3O_4 + O_2 + SO_2 \qquad (C6)$$
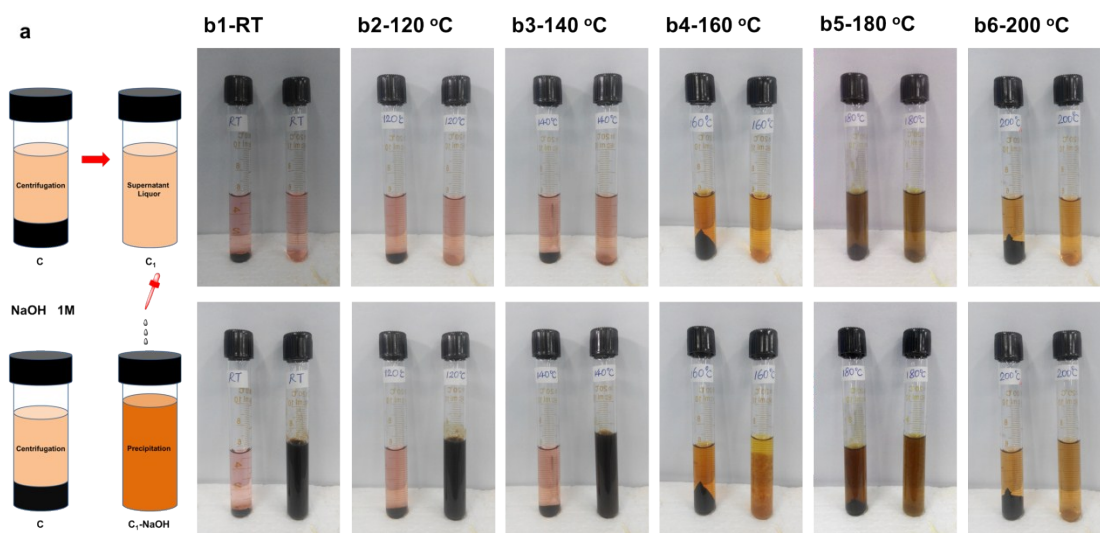
Figure S9. (a) Schematic illustration and (b1-b6) photographs of detecting the concentration of Co^{2+} ions in the reaction process of precursors.

In **Figure S9a**, the schematic illustration of C, C_1 and C_1-NaOH represent the centrifugal sedimentation, clarified centrifugate and sedimentation (by adding NaOH solution) of precursors, respectively. As shown in **Figure S9b1- S9b6**, by the reaction proceeding under different reaction temperatures, the concentration of Co^{2+} ions becomes lower gradually, thus indicating to form the $Co(OH)_2$ microspheres.
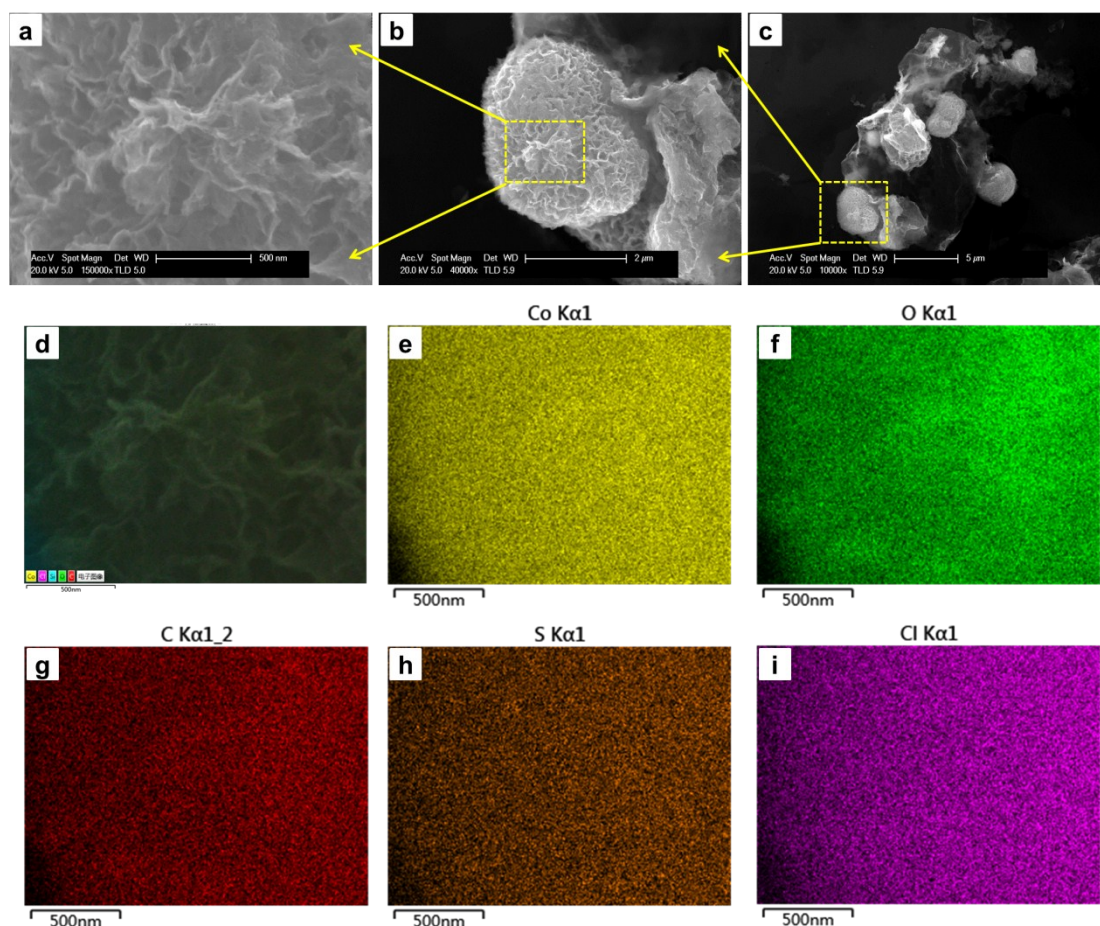
Figure S10. (a-c) Different magnification SEM images of Co_3O_4-G>N-PEGm, (d-i) the EDS elemental mapping analysis of Co-L, O-K, C-K, S-K, and Cl-K for Co_3O_4-G>N-PEGm flower spherses.

The evenly distributed Co, O, C, S and Cl elements (without Na element else) in the Co_3O_4-G>N-PEGm flower microsphere can indicate that the DBS-intercalated $Co(OH)_2$-G>N-PEGm composites have been converted to Co_3O_4-G>N-PEGm with DBS ions doping in the cobalt spinel oxide (Figure S10d-S10i).

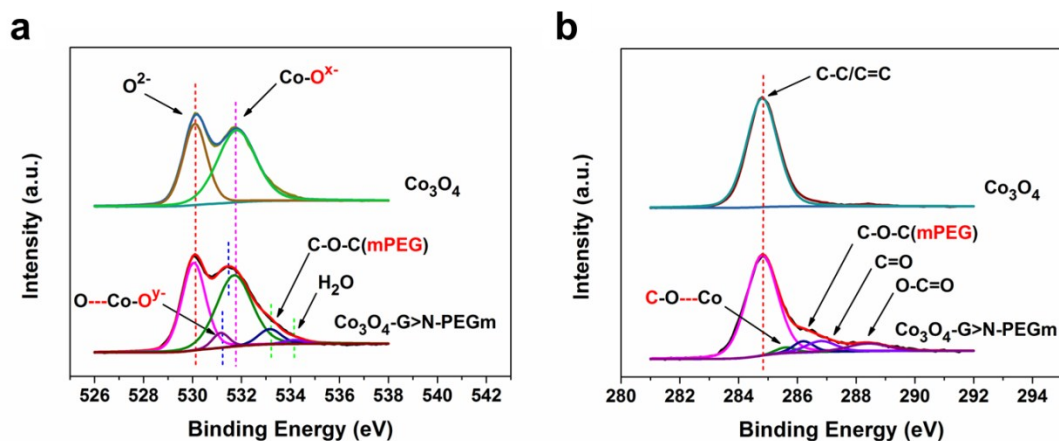**Figure S11.** (a) O 1s and (b) C 1s XPS spectrum of Co_3O_4 and Co_3O_4-G>N-PEGm.

As shown in **Figure S11**b, it displays four different peaks at 284.8, 286.2, 286.8 and 288.4 eV, which can be respectively ascribed to non oxygenated C (C=C/C-C) in aromatic rings (284.8 eV), C in C-O-C (286.2 eV), C in C=O (286.8 eV) and C in O-C=O (288.4 eV) bonding compared with the bare Co_3O_4 flower spheres. The peak at 286.0 eV for Co_3O_4-G>N-PEGm can be mainly attributed to the ether-oxygen groups (C-O-C) of mPEG polymer chains on G>N-PEGm. It is worthy to note that the peak at 285.6 eV for Co_3O_4-G>N-PEGm may correspond to Co←:O-C coordination bonds.
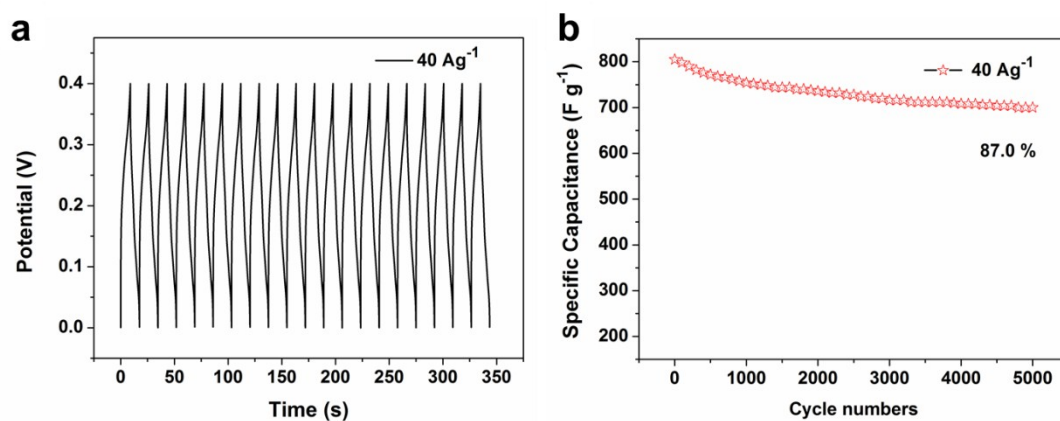
Figure S12. The the long-term stability of Co_3O_4-G>N-PEGm: (a) the initial 20 times galvanostatic charge-discharge curves, and (b) the cycling performance at a current density of 40 Ag^{-1}.

Table S2. BET surface area, pore volume, and BJH pore size distribution of Co_3O_4-G>N-PEGm-250, Co_3O_4-G>N-PEGm-350 and Co_3O_4-G>N-PEGm-450.

Name	BET (m²/g)	Pore volume (mL/g)	BJH (nm)	
Co_3O_4 -G>PEGm-250	107.79	0.52	4	20-40
Co_3O_4 -G>PEGm-350	96.59	0.47	4	25-50
Co_3O_4 -G>PEGm-450	73.08	0.44	6.5	30-65

Figure S13. Photographs of 3D rGO-CNT>N-PEGm aerogels in different sizes.
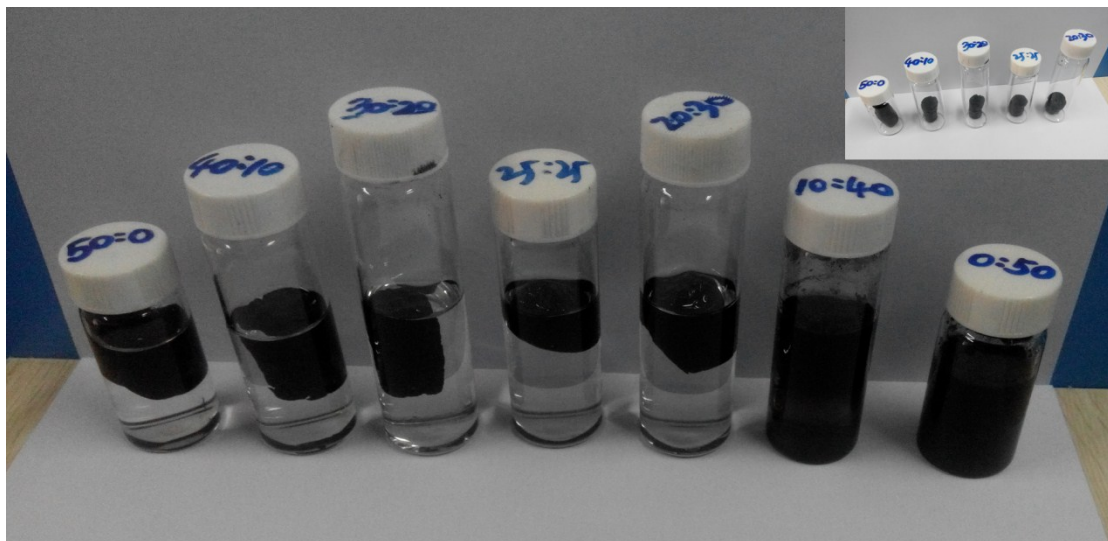
Figure S14. Photographs of 3D rGO-CNT>N-PEGm hydrogels in water with different ratios of rGO-CNT>N-PEGm respectively from left to right as shown on samples (the inset without water).
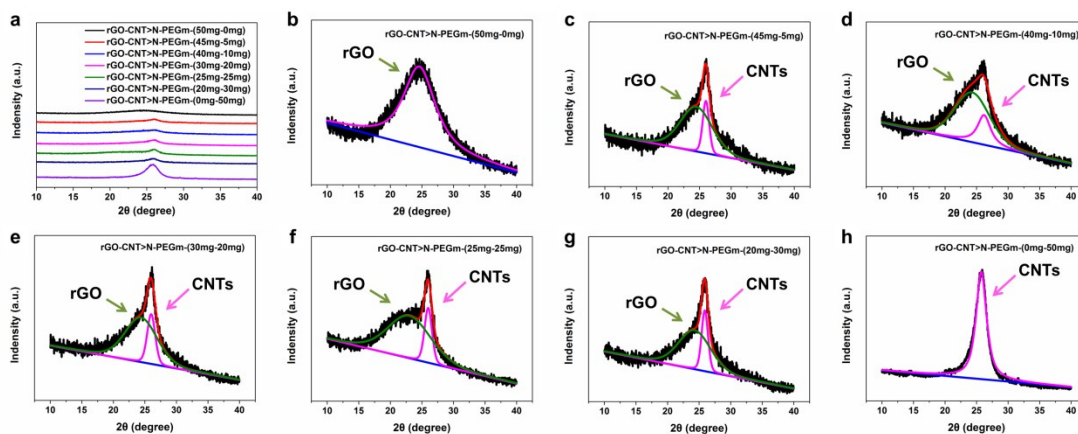
Figure S15. (a) XRD patterns of 3D rGO-CNT>N-PEGm aerogels with different mass ratios. (b-h) XRD peaks of 3D rGO-CNT>N-PEGm aerogels with different ratios according to the (002) planes of rGO and CNTs.

Figure S16. (a-f) and (i-j) TEM images of 3D rGO aerogels. (g-h) and (k-l) HRTEM images of 3D rGO aerogels.

Figure S17. (a-f) and (i-j) TEM images of 3D rGO-CNT>N-PEGm aerogels. (g-h) and (k-l) HRTEM images of 3D rGO-CNT>N-PEGm aerogels.

Figure S18. The electrochemical properties of 3D rGO-CNT>N-PEGm aerogels with various mass ratios (according to rGO / CNT>N-PEGm): (a) CV curves at a scan rate of 100 mV s^{-1}. (b)

Galvanostatic charge-discharge curves at current density of 2 A g^{-1}. (c) The specific capacitance at various current d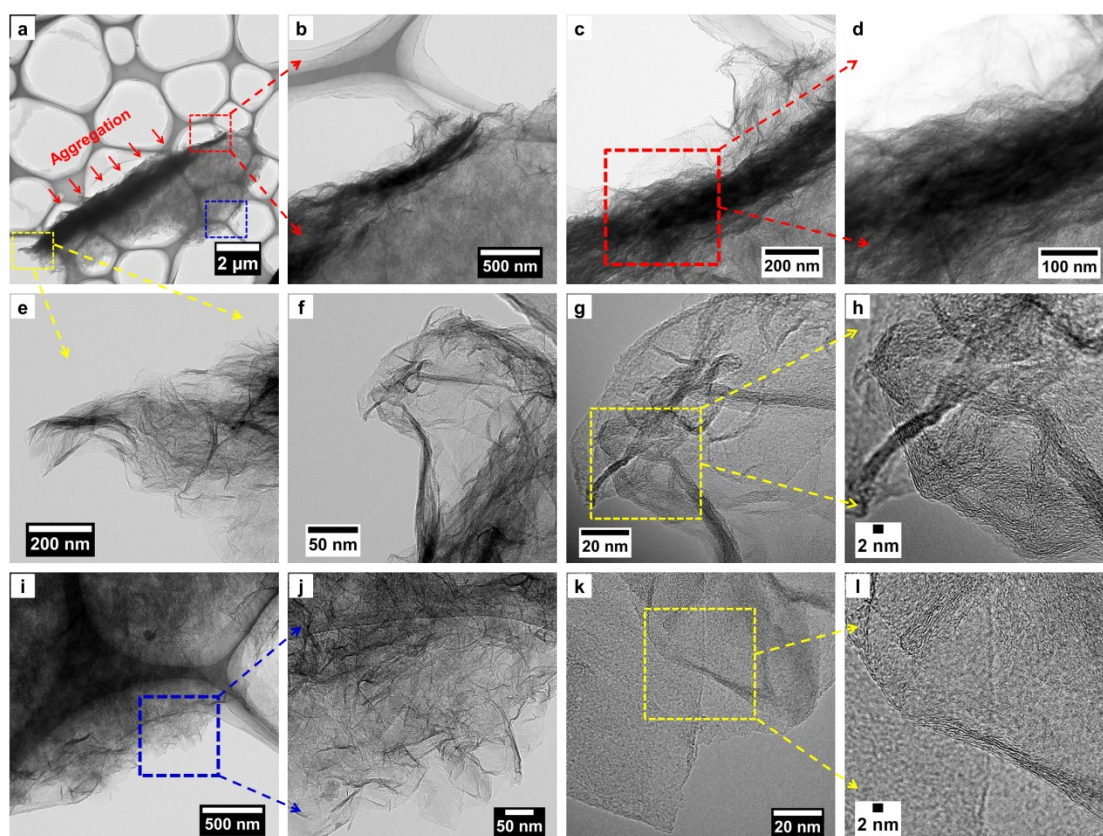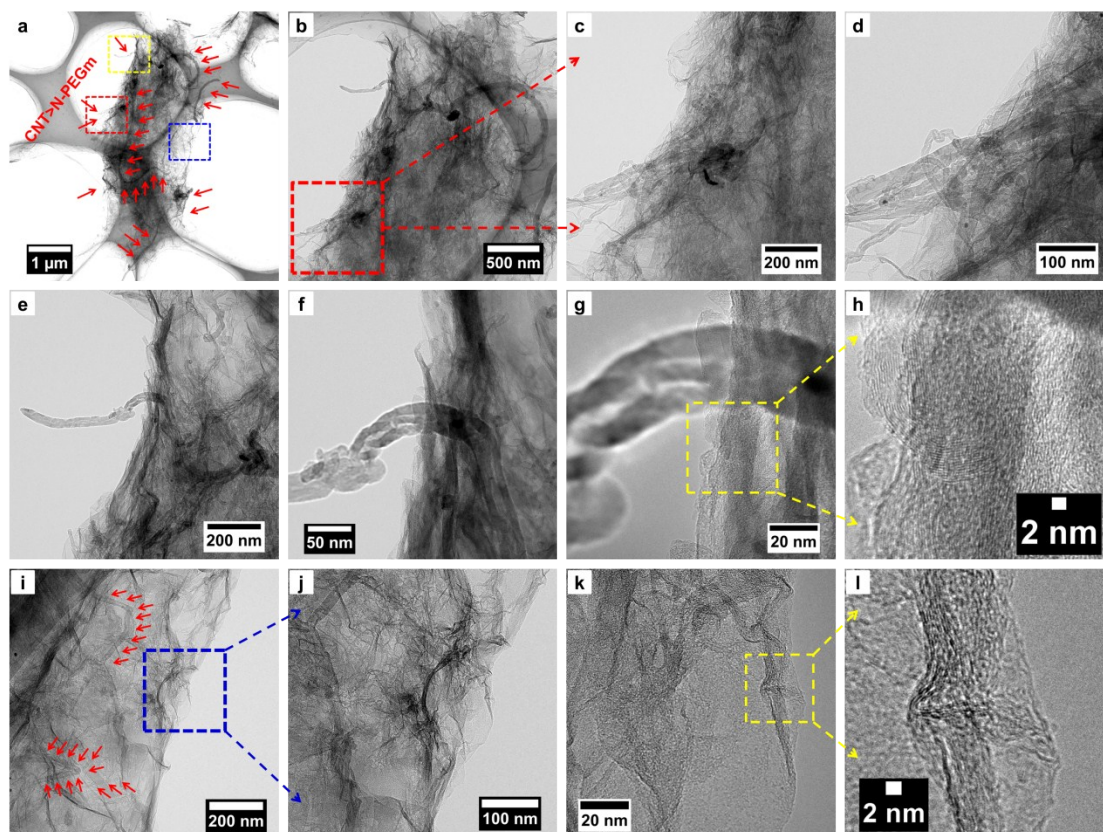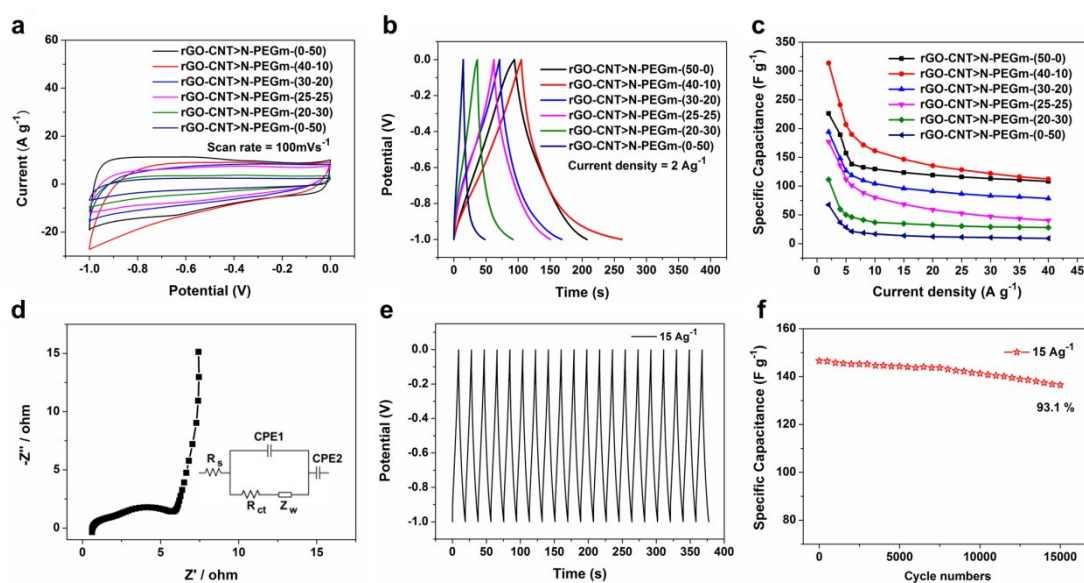ensities. The electrochemical properties of 3D rGO-CNT>N-PEGm aerogels (rGO / CNT>N-PEGm = 40:10): (d) Nyquist plots (the inset shows the equivalent circuit), (e) the initial 20 times galvanostatic charge-discharge curves, and (f) the cycling performance at a current density of 15 A g^{-1}.
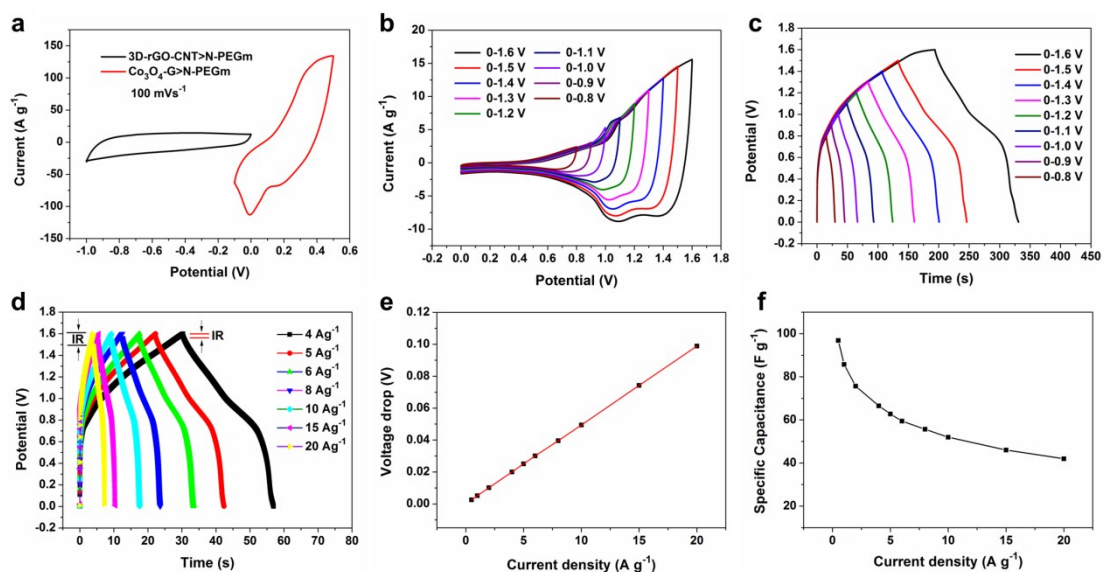
Figure S19. (a) CV curves of 3D rGO-CNT>N-PEGm aerogels and Co$_3$O$_4$-G>N-PEGm electrodes performed in a three-electrode configuration in 6 M KOH solution at a scan rate of 100 mV s^{-1}. (b) CV curves of the asymmetric supercapacitors measured at different potential windows (at 100 mV s^{-1}). (c) Galvanostatic charge-discharge curves with the increase of the potential window (at current density of 1 A g^{-1}). (d) The IR drop at the start point of the discharge curves of Co$_3$O$_4$-G>N-PEGm // rGO-CNT>N-PEGm asymmetric supercapacitors. (e) The voltage drop (IR drop) of Co$_3$O$_4$-G>N-PEGm // rGO-CNT>N-PEGm asymmetric supercapacitors. (f) The specific capacitance at various current densities.

Figure S19b shows a series of CV curves measured with different potential windows from 0-0.8 V to 0-1.6 V at 100 mV s^{-1}. At the operating potential window of 1.0 V, the pseudocapacitive redox-peaks in the region from 0.6 to 1.0 V are attributed to the reversible Faradaic redox reactions of the Co$_3$O$_4$-G>N-PEGm positive electrode

material. When the operating potential window increases to 1.6 V, more redox reactions occure for the larger current response. In **Figure S19c**, the galvanostatic charge-discharge curves are measured with the increase of the potential window at current density of 1 A g^{-1}, which correspond to the CV curves of **Figure S19b** with different potential windows. Moreover, they also combine the pseudocapacitance of Co$_3$O$_4$-G>N-PEGm and electrical double-layer capacitance of the 3D rGO-CNT>N-PEGm aerogels.

Table S3. Comparison of the electrochemical properties of the reported cobalt-based electrodes

Positive electrode	morphology (structure)	Capacit-ance (F g^{-1})	Current density (A g^{-1})	Negative electrode	Energy density (Wh kg^{-1})	Power density (W Kg^{-1})	Reten-tion (%)	Cycle numbers	Ref
Co$_3$O$_4$@CoWO$_4$ /rGO	core/shell nanoneedles	384.7	0.5	rGO	19.1	531.2	88.8	5000	Ref.1
Co$_3$O$_4$@MnO$_2$	core/shell arrays	560	0.2	MEGO	17.7	158	81.1	10, 000	Ref.2
Co$_3$O$_4$-RGO	aerogel	660	0.5	porous carbon	40.65	340	92.92	2000	Ref.3
Co$_3$O$_4$/rGO	nanoflakes	1112	3.3	AC	23.3	2300	-	20, 000	Ref.4
Co$_3$O$_4$/Co$_3$(VO$_4$)$_2$	hybrid nanorods	847.2	1	AC	38	275	94.7	5000	Ref.5
Ni$_x$Co$_{3x}$O$_4$	nanowire array	1479	1	AC	37.4	163	82.8	3000	Ref.6
Co$_3$O$_4$	MOF (ZIF-67)	504	5 mVs^{-1}	nanoporous carbon	36	8000	89	2000	Ref.7
Co$_3$O$_4$@Ni(OH)$_2$	core-shell	15.83 F cm^{-2}	2.5 mA cm^{-2}	rGO	41.90	36.10	-	-	Ref.8
TiO$_2$@C/ Co$_3$O$_4$	ternary hybrid nanocomposites	396.2	1	AC	18.54	222.56	84.6	5000	Ref.9
NCA/Co$_3$O$_4$	in situ coating method	616	1	carbon aerogel	33.43	375	92.5	5000	Ref.10
Co$_3$O$_4$@NiMoO$_4$	nanocomposites	2041	0.5	AC	41.9		68.7	1000	Ref.11
Co$_3$O$_4$@CoMoO$_4$	on Ni foam	857			38		94.2		
Co$_3$O$_4$@NiMoO$_4$	nanosheets array	1526	3 mA cm^{-2}	AC	37.8	482	-	-	Ref.12
Co$_3$O$_4$/rGO	nanocomposite	636	1	AC	35.7	225	95	1000	Ref.13
Co$_3$O$_4$	nanowires (on Ni foam)	278.4	1	CS aerogel	17.9	750	85	1000	Ref.14
Co$_3$O$_4$	nanowire on Ni foam	1217.4	0.7	AC	34	225	~87.7	1500	Ref.15
Co$_3$O$_4$	hollow tube network	1498	0.5	AC	29.5	104	91.4	1000	Ref.16
Co$_3$O$_4$ -G>N-PEGm	3D flower-like microspheres	1625.6	0.5	3D GCA	34.4	400	84.7	10, 000	Our work

MEGO: activated microwave exfoliated graphite oxide activated graphene.

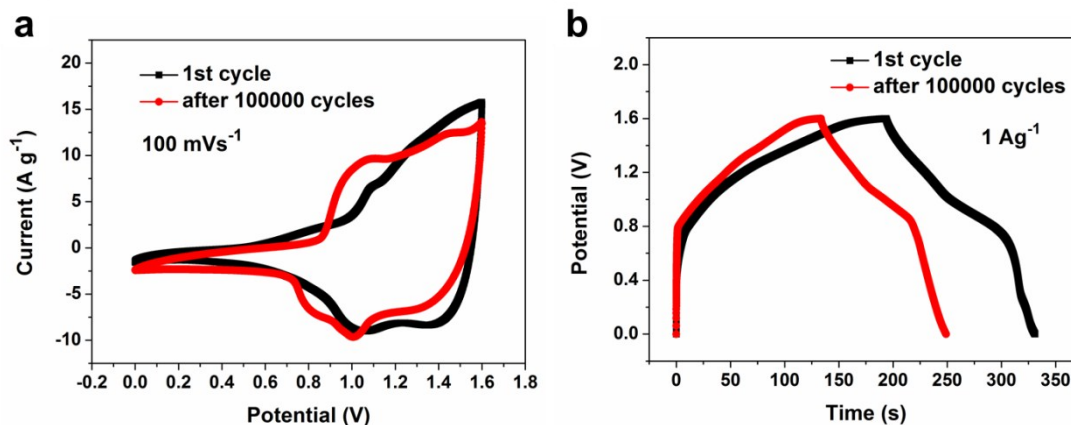CS aerogel: carbon aerogel microspheres.

3D GCA: 3D rGO-CNT>N-PEGm aerogels

Figure S20. The CV curves (at the scan rate of 100 mVs^{-1}) and charge-discharge curves (at the current density of 1 Ag^{-1}) of the 1st and 10000th cycle for the asymmetric supercapacitors.

References

[1] X. Xu, Y. Yang, M. Wang, P. Dong, R. Baines, J. Shen, M. Ye, *Ceram. Int.* **2016**, *42*, 10719.

[2] M. Huang, Y. Zhang, F. Li, L. Zhang, Z. Wen, Q. Liu, *J. Power Sources* **2014**, *252*, 98.

[3] L. Xie, F. Su, L. Xie, X. Li, Z. Liu, Q. Kong, X. Guo, Y. Zhang, L. Wan, K. Li, C. Lv, C. Chen, *Chemsuschem* **2015**, *8*, 2917.

[4] M. Qorbani, T. C. Chou, Y. H. Lee, S. Samireddi, N. Naseri, A. Ganguly, A. Esfandiar, C. H. Wang, L. C. Chen, K. H. Chen, A. Z. Moshfegh, *J. Mater. Chem. A* **2017**, *5*, 12569.

[5] W. Zhang, L. Kong, X. Ma, Y. Luo, L. Kang, *J. Power Sources* **2014**, *269*, 61.

[6] X. Wang, C. Yan, A. Sumboja, P. S. Lee, *Nano Energy* **2014**, *3*, 119.

[7] R. R. Salunkhe, J. Tang, Y. Kamachi, T. Nakato, J. H. Kim, Y. Yamauchi, *ACS nano* **2015**, *9*, 6288.

[8] C. Tang, X. Yin, H. Gong, *ACS Appl. Mat. Interfaces* **2013**, *5*, 10574.

[9] M. Kim, J. Choi, I. Oh, J. Kim, *Phys. Chem. Chem. Phys.* **2016**, *18*, 19696.

[10] G. Sun, L. Ma, J. Ran, X. Shen, H. Tong, *J. Mater. Chem. A* **2016**, *4*, 9542.

[11] X. Ma, L. Kong, W. Zhang, M. Liu, Y. Luo, L. Kang, *Electrochim. Acta* **2014**, *130*, 660.

[12] W. Hong, J. Wang, P. Gong, J. Sun, L. Niu, Z. Yang, Z. Wang, S. Yang, *J. Power Sources* **2014**, *270*, 516.

[13] L. Xie, J. Wu, C. Chen, C. Zhang, L. Wan, J. Wang, Q. Kong, C. Lv, K. Li, G. Sun, *J. Power Sources* **2013**, *242*, 148.

[14] W. Liu, X. Li, M. Zhu, X. He, *J. Power Sources* **2015**, *282*, 179.

[15] X. Zhang, Y. Zhao, C. Xu, *Nanoscale* **2014**, *6*, 3638.

[16] J. Li, G. Zan, Q. Wu, *J. Mater. Chem. A* **2016**, *4*, 9097.